Identifying champion nanostructures for solar water splitting

Scott C. Warren[1*†], Kislon Voïtchovsky[2], Hen Dotan[3], Celine M. Leroy[1], Maurin Cornuz[1], Francesco Stellacci[2], Cécile Hébert[4], Avner Rothschild[3], and Michael Grätzel[1]

[1] *Laboratory of Photonics and Interfaces, École Polytechnique Fédérale de Lausanne, Lausanne, Switzerland.*

[2] *Supramolecular NanoMaterials and Interfaces Laboratory, École Polytechnique Fédérale de Lausanne, Lausanne, Switzerland.*

[3] *Department of Materials Science and Engineering, Technion - Israel Institute of Technology, Haifa, Israel.*

[4] *Interdisciplinary Centre for Electron Microscopy, École Polytechnique Fédérale de Lausanne, Lausanne, Switzerland.*

**Correspondence to: scw28@cornell.edu.*

† *Present address: Non-Equilibrium Energy Research Center, Northwestern University, Evanston, IL 60208, USA.*

Charge transport in nanoparticle-based materials underlies many emerging energy conversion technologies, yet assessing the impact of nanometer-scale structure on charge transport across micron-scale distances remains a challenge. Here we develop an approach for correlating the spatial distribution of crystalline and current-carrying domains in entire nanoparticle aggregates. We apply this approach to nanoparticle-based α-Fe_2O_3 electrodes that are of interest in solar-to-hydrogen energy conversion. In correlating structure and charge transport with nanometer resolution across micron-scale distances, we have identified the existence of champion nanoparticle aggregates that are most responsible for the high photoelectrochemical activity of the present electrodes. Indeed, when electrodes are fabricated with a high proportion of these champion nanostructures, the electrodes achieve the highest photocurrent of any metal oxide photoanode for photoelectrochemical water splitting under 100 mW cm^{-2} air mass 1.5 global sunlight.

Batteries, fuel cells, and solar energy conversion devices have emerged as a class of important technologies that increasingly rely upon electrodes derived from nanoparticles[1]. These nanoparticle-based materials provide a unique challenge in assessing structure-property relationships because of the disordered arrangement of nanocrystals that results when nanoparticles collide and aggregate[2-6]. The morphological evolution that follows aggregation further obscures the influence of particle size, shape, and interfacial characteristics in defining the physical properties of these materials[7,8]. For the nanoparticle-based electrodes used in solar energy conversion, structural defects such as grain boundaries define pathways for charge transport by creating potential barriers and by promoting recombination[9]. Because of the complexity of these materials, within a single electrode there may exist a small proportion of "champion" nanostructures—by analogy with champion solar cells[10,11], these are nanostructures that provide the highest solar conversion efficiencies—that contribute the majority of the electrode's photocurrent. Further improvement of device performance requires an analytical

approach that identifies these champion nanostructures, quantitatively relating their microstructural features to their charge transport characteristics.

Among the nanoparticle-based electrodes used in solar water splitting, α-Fe_2O_3 (hematite) has emerged as one of the most promising materials[12-23]. Hematite is attracting broad interest for use in water photoelectrolysis for hydrogen production because iron is one of the least expensive and most abundant metals and hematite has a high theoretical solar-to-hydrogen conversion efficiency of 14 to 17%, which corresponds to a photocurrent of 11 to 14 mA cm^{-2} [24]. In spite of performance improvements to as high as 3 mA cm^{-2} under standard air mass (AM) 1.5 illumination[13,25], it has remained a challenge to identify the structural characteristics of hematite nanoparticle aggregates that most influence performance. In particular, although it has been proposed that the synthesis of nanostructures with increasingly small dimensions will improve photocurrent by decreasing electron-hole recombination[17,25], little is known about the influence of the structural defects that accompany such nanostructuring strategies.

The hematite electrodes used in this study were prepared by vapor phase deposition of an iron oxide aerosol onto a heated fluorine-doped tin oxide (FTO) substrate; in a previous study it was found that deposition at higher gas flow rates and substrate temperatures produced electrodes with improved photocurrents. In this study, we compare electrodes prepared at heater set temperatures/air flow rates of 475 °C/2 L min^{-1} (hereafter labelled "2L") and 545 °C/6 L min^{-1} (labelled "6L")[26]. Because the flow of air cools the substrate, the surface temperatures of the two samples are 415 and 425 °C, respectively. The electrodes used here were aged one month in air at room temperature followed by electrochemical cycling in the dark for two hours from 0.7 to 1.7 V *vs.* RHE, during which an improvement in photocurrent occurred (see Supplementary Information for further details). Light intensity readings were taken before and after the cycling to ensure that instrument drift did not influence measurements.

Photoelectrochemical measurements under AM 1.5G light achieved a photocurrent for water splitting (water oxidation to oxygen gas on the hematite photoanode, water reduction on a platinum counter electrode) of 4.0 ± 0.1 mA cm^{-2} at 1.53 V *vs.* RHE (Fig. 1) for the 6L electrode, the highest yet achieved for hematite as well as any metal oxide photoanode. The 2L sample produced a photocurrent of 2.6 ± 0.1 mA cm^{-2} at 1.53 V *vs.* RHE. The improved photocurrent with ageing was observed in all samples and was typically 22 ± 2% in the 6L electrodes and 26 ± 3% in the 2L electrodes.

To account for the different photocurrents between the 2L and 6L electrodes, we began an analysis of electrode structure using traditional characterization techniques, including SEM (Fig. 2a,b), bright-field transmission electron microscopy (BF-TEM) (Fig. 2c-f), and powder x-ray diffraction (PXRD). The electrodes were composed of separated aggregates of nanoparticles, each of which exhibited a tree-like structure[13]. SEM, BF-TEM, and PXRD measurements found small or statistically insignificant structural differences between the 2L and 6L samples. For example, the difference between 2L and 6L areal densities and lengths of nanoparticle aggregates were statistically insignificant. A gradient in particle size was observed for the 2L / 6L electrodes of 30 ± 3 nm / 35 ± 4 nm for particles at the base of aggregates (near the substrate) to 5 ± 1 nm / 10 ± 2 nm for particles at the tip of aggregates. PXRD also showed that the Scherrer domain size was 24 ± 2 nm / 29 ± 3 nm for 2L / 6L and that the crystallites in these electrodes were almost randomly oriented (Supplementary Fig. S22).

Despite the small particle and domain sizes, high resolution TEM (HR-TEM) revealed that lattice fringes with similar orientations extended for hundreds of nanometers across the nanoparticle aggregates (Supplementary Fig. S24). Quantitative analysis of crystallinity by HR-TEM was impossible, however, because of the varying thickness of the nanoparticle aggregates, the overlap of multiple crystallites, and the small area that could be visualized simultaneously at high resolution. While HR-TEM is useful in providing information about a material's microstructure, the small volume of the material that is probed makes it difficult to systematically assess the impact of microstructure on micron-scale charge transport in polycrystalline nanoparticle percolation networks.

We therefore developed a two-part strategy that relies on: (1) experiments that correlate the spatial distribution and orientation of crystallites within entire nanoparticle aggregates with the size and shape of the percolation networks that conduct majority carriers (Fig. 3) and (2) a new theoretical model that quantitatively assesses the impact of crystal-crystal interfaces—i.e., grain boundaries—on the experimentally measured photocurrent. In the first part of our strategy, we adapt a dark field TEM (DF-TEM) method based on the crystal-by-crystal imaging of entire nanocrystal aggregates, which provides information about the spatial distribution of high and low angle grain boundaries (Fig. 3a). By using conducting atomic force microscopy (C-AFM), we measure the majority carrier charge transport characteristics of these nanoparticle aggregates (Fig. 3b). The DF-TEM images, by themselves, allow the extent of minority charge carrier recombination at grain boundaries to be estimated. In combination with the C-AFM analysis, we demonstrate that it is possible to identify the types of grain boundaries that most influence majority charge carrier transport. In the second part of our strategy, we develop a model for the photocurrent that relates the most important structural features of grain boundaries—namely, their prevalence within nanostructures and their surface state concentration—to the experimentally measured photocurrent (Fig. 1). Because the model allows for a quantitative comparison of previously disparate experimental observations, it provides a powerful test for whether these structural features need to be invoked to understand charge transport processes in complex, nanostructured materials.

To distinguish and accurately image complex crystals by DF-TEM, we have searched for regions in these nanoparticle aggregates where the crystallites do not overlap. The diffraction patterns acquired from non-overlapping regions are used to determine crystal orientation and are further used to create DF-TEM images of the entire crystallite. This is repeated for each region with a distinct orientation. Subsequently, we colorized and merged the dark field images to map crystallite orientation within the nanoparticle aggregates (see Supplementary Information for a full description of methods and additional data). By distinguishing overlapping crystals, this new DF-TEM technique provides some of the information content achieved by three-dimensional DF-TEM[27] while retaining the simplicity of traditional two-dimensional DF-TEM[28,29].

Using this approach, we first examined the 2L hematite nanoparticle aggregates (Fig. 4a-f). A representative aggregate is analysed, showing the BF-TEM image (Fig. 4a), diffraction pattern (Fig. 4b), and composite DF-TEM image (Fig. 4c). The observation of several diffraction patterns revealed that multiple crystal orientations were present. The DF-TEM images provided a spatial resolution of 1.2 nm, which was sufficient to examine the smallest nanoparticles present in the electrodes. Most notable in Fig. 4c are the large regions with similar crystallographic orientation that extend for up to 400 nm. The size mismatch between these regions and the Scherrer domain size suggests that these regions are not single crystals but are mosaics of

nanocrystals with similar but not identical orientations (see Supplementary Fig. S1 for a discussion of terminology). The smearing of the diffraction spots into incomplete rings by as much as 14° (see, *e.g.*, the 220 reflection in Fig. 4b and Supplementary Fig. S23) and HR-TEM images with high concentrations of edge dislocations (Supplementary Fig. S24) further supports this conclusion. Each region with similar orientation appears contiguous (Supplementary Fig. S6), which is consistent with growth by oriented attachment[3,6].

Within the 2L electrodes, a second, less common type of aggregate was also observed (Fig. 3d-f). Instead of containing several distinct mosaics (Fig. 3c), these aggregates comprised a single mosaic—*i.e.*, a single principle orientation of nanocrystals (Fig. 3e). When a DF image was created from a single diffraction spot, only a portion of the aggregate was imaged (Fig. 3f). To image the entire length of the mosaic, four diffraction spots were used. The need to use multiple diffraction spots typically arises when there is a small amount of bending (a few mrads) across a nanostructure. This can arise from the presence of small angle grain boundaries throughout the mosaic, although bending induced by sample preparation cannot be entirely ruled out.

This analysis was applied to the 6L hematite electrodes (Fig. 4g-j). Several nanoparticle aggregates were analysed in each image and, as before, evidence for rotation was observed within the diffraction patterns and DF images, indicating that these mosaics are also not a single crystal. The composite DF images (Fig. 4h,j) reveal that the most significant difference between 2L and 6L samples is that there are many fewer mosaics per nanoparticle aggregate, on average, in the 6L sample. An analysis of 17 nanoparticle aggregates from the 6L sample revealed that 82% of the aggregates had a single principal crystallographic orientation and that 18% had two or more orientations. In comparison, we examined 40 nanoparticle aggregate structures in the 2L sample, which revealed that only 25% of the aggregates had a single principal orientation and that 75% had two or more orientations. The difference in the number of high angle grain boundaries per nanoparticle aggregate is statistically significant: the probability that a test-statistic is at least as extreme as the one observed, p, is 6.0×10^{-5}.

We hypothesized that high angle grain boundaries could decrease photocurrent in two ways: first, because these grain boundaries have a high concentration of interface states, they may act as recombination centers[30]; second, the grain boundaries can generate a potential barrier that blocks majority carrier charge transport between adjacent crystals[31]. In the present materials the relatively small volume fraction of the hematite that is near a high angle grain boundary—*i.e.*, within a typical diffusion and drift delivery length of 2 to 10 nm[32]—suggests that the first possibility does not explain most of the difference in photocurrent between 2L and 6L electrodes. Instead, we focus on the possible formation of potential barriers at the grain boundaries.

These potential barriers can limit photocurrent *via* two mechanisms. First, thermionic emission over potential barriers formed at high angle grain boundaries limits majority carrier transport[31] and, second, the potential drop at high angle grain boundary barriers decreases the potential that falls at the electrode-electrolyte interface. The first effect could limit current transport through large regions and effectively render them inactive for water splitting. The second effect, which has not previously been described for water splitting photoelectrodes, could be especially significant in hematite because photocurrent generation primarily relies on light absorbed within the electrode-electrolyte space charge layer[12], the width of which increases with the square root of the potential that falls within this layer[33]. The possibility that potential barriers at high angle grain boundaries in the present electrodes limit charge transport is consistent with

earlier electrical transport measurements on sintered polycrystalline hematite with a similar charge carrier density, for which a grain boundary potential barrier of 0.7 eV was found[34]. A barrier height of this magnitude is expected to limit charge transport for the voltages that these electrodes experience under typical conditions.

To examine whether grain boundaries impede electron transport in these electrodes, we performed several types of electrical conductivity measurements. First, to determine whether charge transport can occur directly between neighbouring tree-like nanoparticle aggregates, we grew hematite on insulating substrates (glass and sapphire) and performed van der Pauw electrical conductivity measurements (see Supplementary Information for full details). For all samples, the measured resistance exceeded the dynamic range of our ohm-meter, suggesting an in-plane conductivity of less than 10^{-8} S cm^{-1}. This is significantly lower than the intrinsic conductivity of the present samples, 0.3 S cm^{-1}, suggesting that electrical transport does not occur between most adjacent nanoparticle aggregates.

The absence of lateral electrical transport between adjacent nanoparticle aggregates suggested that the vertical charge transport properties of individual nanoparticle aggregates grown on FTO could be probed by conducting atomic force microscopy (C-AFM, Fig. 3b). In C-AFM, an electrically conductive tip is placed in contact with the nanoparticle aggregates, thereby completing a circuit and allowing the charge transport properties of single aggregates to be probed. If high angle grain boundaries create large potential barriers in these electrodes, the size of the current-carrying regions and the magnitude of current passing through them should correlate with the structural features observed by DF-TEM (Fig. 3). We hypothesized that such a DF-TEM/C-AFM approach, when performed on a sufficiently large number of nanostructures, would allow inferences to be made about the impact of microstructural features on macroscopic properties—namely, the water splitting characteristics of these electrodes as shown in Fig. 1.

The C-AFM experiment acquired topography and current maps with nanometer and picoampere to nanoampere resolution over multiple regions of each sample. To carry out a meaningful statistical analysis of the C-AFM data, we investigated ten randomly selected square regions (350 × 350 nm) of each sample. Every location was repetitively scanned, incrementing the applied tip-sample potential by 3 V between successive scans from 0 to 12 V. Representative examples of topography and current maps recorded at 9 V are shown for the 6L (Fig. 5a,b) and 2L electrodes (Fig. 5d,e). The measurements reveal that regions of high and low current can be observed in each sample and that there is correspondence between topographic features and regions with similar current transport.

The sizes of regions with similar current differed greatly between the 2L and 6L electrodes: in electrode 2L, regions with similar current were typically smaller than 60 nm but in electrode 6L they were between 60 and 200 nm. These sizes are much larger than the 5-10 nm nanoparticles at the tip of the aggregates but are similar to the size of the nanocrystalline mosaics in each sample (Fig. 4). These observations provide additional evidence that current transport is mediated primarily by high angle grain boundaries rather than low angle grain boundaries—thereby implying that many or most of the high angle grain boundaries create potential barriers that limit current transport. Moreover, a qualitative comparison of these representative current maps also shows that charge transport in the 2L sample is substantially slower than the 6L sample. This result is expected for materials in which the primary distinction is the presence or absence of high angle grain boundaries with potential barriers.

The topographic and current maps did not significantly depend on the scan direction or tip work function (gold and platinum were used), and appeared reproducible at higher voltages: successive scans at 6, 12, and 6 V showed that the two 6 V images were similar (Supplementary Fig. S10). These control experiments show that the measured currents are not an artifact of sample damage or a locally varying Schottky barrier at the sample-tip contact but instead provide insight into the charge transport within the hematite nanostructures. Indeed, earlier experiments showed that Schottky barriers do not form at gold-hematite interfaces because of Fermi level pinning[17].

To better understand the origin of the observed current variations within an image, we quantified the current transport characteristics in each of the two samples. A useful indicator is the maximum current (I_{max}) measured in either the 2L or 6L electrodes at a given voltage. The current could be directly compared between the two samples because they had similar carrier concentrations and Si doping levels, as determined by ToF-SIMS and Mott-Schottky analysis (see Supplementary Information). Because the electronic mobility of hematite varies with crystal orientation by up to one order of magnitude[35], it may be possible to expect a variation in current by this amount. We therefore set a threshold for the current that is one-tenth the value of I_{max}: below this threshold the limited current is attributed to resistance at grain boundaries. Using this threshold, we found that 99% of the 2L sample had a current limited by grain boundaries *versus* 61% for the 6L sample (Fig. 5g); the ratio of these areas (Fig. 5h) provides an estimate of the relative contribution of grain boundary-limited current. Regardless of the threshold chosen to indicate the presence of grain-boundary limited current (Fig. 5h), the 2L sample always has a larger area dominated by grain boundaries (Fig. 5h). These findings are consistent with DF-TEM measurements, which showed that 75% of the 2L nanoparticle aggregates have high angle grain boundaries as compared to 18% for the 6L electrode. It should be noted that a fully quantitative agreement between the two techniques would be surprising for two reasons. First, only the high angle grain boundaries parallel to the hematite-FTO interface will prevent current transport. Second, the magnitude of a potential barrier is a function of the interface state density and energy[31]: although most high angle grain boundaries have high densities of interface states, there may be a small proportion with relatively low concentrations of interface states[36].

An analysis of the I-V characteristics derived from C-AFM images showed that the 2L and 6L samples exhibit sub- and super-ohmic behavior, respectively (Supplementary Fig. S9). This can be explained by the presence of a higher interfacial trap density at grain boundaries in the 2L sample[31,37], and is also consistent with an increased density of high angle grain boundaries. Although these results have to be considered with caution because the slow wearing of the C-AFM tip that occurs with each scan can introduce a systematic error in the measurements, repeated scans in the same area yielded similar results and suggested that the systematic error was small (Supplementary Fig. S10).

The DF-TEM and C-AFM measurements provide a consistent picture of majority carrier charge transport mediated by high angle grain boundaries. To relate the structure (Fig. 4) and majority carrier current transport characteristics (Fig. 5) to the photocurrent (Fig. 1), we have developed the first model (Supplementary Information) that takes into account the ways in which a potential barrier at a grain boundary influences photocurrent in a water splitting device. In this model, thermionic emission across a grain boundary limits majority carrier current and a potential drop at a grain boundary is subtracted from the potential drop within the space charge layer at the electrode-electrolyte interface. The model revealed that in the absence of grain

boundary barriers, a photocurrent of approximately 5 mA cm^{-2} is expected, whereas a sample in which all current must pass over a grain boundary barrier has little or no photocurrent (Fig. 6a). The variation in photocurrent between the 2L and 6L electrodes could be explained within the framework of our model by using a linear combination of these two extremes. The model predicted that approximately 19% of the volume of the 6L sample and 52% of the volume of the 2L sample has grain boundary-limited photocurrent (see Supplementary Information for discussion). Although these models have many free parameters, the calculated photocurrents (Fig. 6b) are qualitatively similar to the experimental results (Fig. 1) and, furthermore, the predicted volume fraction of each electrode that is affected by grain boundary barriers is consistent with DF-TEM and C-AFM analyses of high angle grain boundary concentration. This provides evidence that the potential barriers that are observed in the dark by C-AFM are still present under illumination.

The examination of grain boundary effects in nanocrystalline electrodes, particularly in the context of percolation theory, allows several phenomena that have been previously reported to be re-interpreted within a simpler framework. For example, it has been frequently suggested that the alignment of hematite's high mobility planes perpendicular to the substrate was necessary to achieve good electron transport through the material[13,26,38-40] because a correlation between texturing and photocurrent was observed. A calculation of the potential drop across the bulk in hematite electrodes—about 6 μV—rules out this possibility, however (see Supplementary Information). In fact, Somorjai's hematite single crystals, which were a millimeter thick and had the most conductive planes parallel to the semiconductor-water interface, still achieved an impressive incident photon-to-current efficiency of 30% at a low applied potential[41]. We therefore propose that the correlation between highly textured hematite electrodes and improved photocurrents can be attributed to the removal of high angle grain boundaries with large potential barriers. This is consistent with observations of poor electron transport in polycrystalline hematite electrodes, where it was observed that the photocurrent decreases with increasing film thickness when the film is illuminated through the electrolyte but not when illuminated through the substrate[14,38,42]. This is also consistent with the observation that the photocurrent decreases more rapidly in the 2L samples than the 6L samples with increasing film thickness[25], which again suggests that these samples have fewer grain boundary barriers.

In many nanocrystalline electrodes that are prepared from colloids, the electrode is inactive for water splitting until it is heated to a critical temperature—in the case of hematite, this temperature is usually 800 °C[19,42,43]. We propose that this temperature-dependence can be explained, in part, by considering the role of grain boundaries. Only when sufficient thermal energy is provided to re-orient adjacent grains, activate dopants, or move passivating species to grain boundaries will the potential barriers at high angle grain boundaries be lowered sufficiently such that a percolation network that facilitates electronic transport can form. To test this hypothesis and generalize the conclusions of our model, we prepared electrodes from colloidal particles with several different carrier concentrations and interfacial state densities (Supplementary Information), which are the two parameters that most influence the formation of potential barriers[44]. When the doping level is low and the interface state concentration is high, large potential barriers are expected to form; conversely, high doping levels and low interface state concentrations yield negligible barriers[44]. These predictions agreed with the experimentally measured photocurrent and charge transport characteristics measured by C-AFM (Supplementary Information). From these experiments, we conclude that both the orientation and interface state density of adjacent nanoparticles must be controlled to maintain low potential barriers at grain

boundaries. In particular, percolation pathways through nanocrystalline electrodes will occur only when interface traps are passivated, when nanocrystals are depleted of charge carriers, or when high angle grain boundaries are entirely removed from the material (Supplementary Information).

In conclusion, we have developed a combined DF-TEM and C-AFM approach for examining nanocrystalline mosaics in which grain boundaries and current transport are visualized with nanometer spatial resolution across micrometer distances. This allows meaningful information to be extracted from materials with high structural complexity. It is likely that even further insight will be gained by extending the analysis using three dimensional orientational imaging[27], although the relative simplicity of the DF-TEM technique developed here is compelling. Our studies suggest that there are champion nanoparticle aggregates that are largely responsible for the high photocurrent in the present samples. These champion nanoparticle aggregates may have photon-to-current efficiencies approaching the theoretical limit. If the structural properties of these aggregates can be more fully understood, it is likely that the performance gap between the new benchmark reported in this work and the maximum theoretical efficiency can be bridged. More generally, we have shown how the structural variations that naturally arise in materials derived from nanoparticles provide an exciting opportunity to identify those structures that enable champion performance.

References

1 Arico, A. S., Bruce, P., Scrosati, B., Tarascon, J.-M. & van Schalkwijk, W. Nanostructured Materials for Advanced Energy Conversion and Storage Devices. *Nat. Mater.* **4**, 366-377 (2005).

2 Warren, S. C. *et al.* Ordered Mesoporous Materials from Metal Nanoparticle-Block Copolymer Self-Assembly. *Science* **320**, 1748-1752 (2008).

3 Penn, R. L. & Banfield, J. F. Imperfect Oriented Attachment: Dislocation Generation in Defect-Free Nanocrystals. *Science* **281**, 969-971 (1998).

4 Banfield, J. F., Welch, S. A., Zhang, H., Ebert, T. T. & Penn, R. L. Aggregation-based crystal growth and microstructure development in natural iron oxyhydroxide biomineralization products. *Science* **289**, 751-754 (2000).

5 Zheng, H. *et al.* Observation of Single Colloidal Platinum Nanocrystal Growth Trajectories. *Science* **324**, 1309-1312 (2009).

6 Li, D. *et al.* Direction-Specific Interactions Control Crystal Growth by Oriented Attachment. *Science* **336**, 1014-1018 (2012).

7 Ostwald, W. *Lehrbuch der allgemeinen chemie*. Vol. 2 (1896).

8 Schliehe, C. *et al.* Ultrathin PbS sheets by two-dimensional oriented attachment. *Science* **329**, 550-553 (2010).

9 Seager, C. H. & Ginley, D. S. Passivation of grain boundaries in polycrystalline silicon. *Appl. Phys. Lett.* **34**, 337-340 (1979).

10 Green, M. A., Emery, K., Hishikawa, Y., Warta, W. & Dunlop, E. D. Solar cell efficiency tables (version 39). *Progress in Photovoltaics: Research and Applications* **20**, 12-20 (2012).

11 Grätzel, M. Photovoltaic and photoelectrochemical conversion of solar energy. *Philosophical Transactions of the Royal Society A: Mathematical, Physical and Engineering Sciences* **365**, 993-1005 (2007).

12 Dotan, H., Sivula, K., Graetzel, M., Rothschild, A. & Warren, S. C. Probing the photoelectrochemical properties of α-Fe_2O_3 electrodes using hydrogen peroxide (H_2O_2) as a hole scavenger. *Energy Environ. Sci.* **4**, 958-964 (2011).

13 Kay, A., Cesar, I. & Gratzel, M. New benchmark for water photooxidation by nanostructured α-Fe_2O_3 films. *J. Am. Chem. Soc.* **128**, 15714-15721 (2006).

14 Spray, R. L. & Choi, K.-S. Photoactivity of transparent nanocrystalline Fe_2O_3 electrodes prepared via anodic electrodeposition. *Chem. Mater.* **21**, 3701-3709 (2009).

15 Wang, H., Deutsch, T. & Turner, J. A. Direct water splitting under visible light with nanostructured hematite and WO_3 photoanodes and a $GaInP_2$ photocathode. *J. Electrochem. Soc.* **155**, F91-F96 (2008).

16 Jang, J. S., Yoon, K. Y., Xiao, X., Fan, F.-R. F. & Bard, A. J. Development of a potential Fe_2O_3-based photocatalyst thin film for water oxidation by scanning electrochemical microscopy: effects of Ag-Fe_2O_3 nanocomposite and Sn doping. *Chem. Mater.* **21**, 4803-4810 (2009).

17 Thimsen, E., Leformal, F., Graetzel, M. & Warren, S. C. Influence of plasmonic Au nanoparticles on the photoactivity of Fe_2O_3 electrodes for water splitting. *Nano Lett.* **11**, 35-43 (2011).

18 Beermann, N., Vayssieres, L., Lindquist, S. E. & Hagfeldt, A. Photoelectrochemical studies of oriented nanorod thin films of hematite. *J. Electrochem. Soc.* **147**, 2456-2461 (2000).

19 Kleiman-Shwarsctein, A., Hu, Y.-S., Forman, A. J., Stucky, G. D. & McFarland, E. W. Electrodeposition of α-Fe_2O_3 Doped with Mo or Cr as Photoanodes for Photocatalytic Water Splitting. *J. Phys. Chem. C* **112**, 15900-15907 (2008).

20 Lin, Y., Zhou, S., Sheehan, S. W. & Wang, D. Nanonet-based hematite heteronanostructures for efficient solar water splitting. *J. Am. Chem. Soc.* **133**, 2398-2401 (2011).

21 van de Krol, R., Liang, Y. Q. & Schoonman, J. Solar hydrogen production with nanostructured metal oxides. *J. Mater. Chem.* **18**, 2311-2320 (2008).

22 Warren, S. C. & Thimsen, E. Plasmonic solar water splitting. *Energy Environ. Sci.* **5**, 5133-5146 (2012).

23 Dotan, H. *et al.* Resonant light trapping in ultrathin films for water splitting. *Nat. Mater.* **12**, 158-164 (2013).

24 Marusak, L. A., Messier, R. & White, W. B. Optical absorption spectrum of hematite, α-Fe_2O_3 near IR to UV. *J. Phys. Chem. Solids* **41**, 981-984 (1980).

25 Tilley, S. D., Cornuz, M., Sivula, K. & Grätzel, M. Light-Induced Water Splitting with Hematite: Improved Nanostructure and Iridium Oxide Catalysis. *Angew. Chem. Int. Ed.* **49**, 6405-6408 (2010).

26 Cornuz, M., Grätzel, M. & Sivula, K. Preferential orientation in hematite films for solar hydrogen production via water splitting. *Chem. Vap. Deposition* **16**, 291-295 (2010).

27 Liu, H. H. *et al.* Three-Dimensional Orientation Mapping in the Transmission Electron Microscope. *Science* **332**, 833-834 (2011).

28 Dingley, D. J. Orientation Imaging Microscopy for the Transmission Electron Microscope. *Microchim. Acta* **155**, 19-29 (2006).

29 Huang, P. Y. *et al.* Grains and grain boundaries in single-layer graphene atomic patchwork quilts. *Nature* **469**, 389-392 (2011).
30 Shockley, W. & Read, W. T. Statistics of the Recombinations of Holes and Electrons. *Phys. Rev.* **87**, 835 (1952).
31 Pike, G. E. & Seager, C. H. The dc voltage dependence of semiconductor grain-boundary resistance. *J. Appl. Phys.* **50**, 3414-3422 (1979).
32 Kennedy, J. H. & Frese, K. W., Jr. Photooxidation of water at α-Fe_2O_3 electrodes. *J. Electrochem. Soc.* **125**, 709-714 (1978).
33 Memming, R. *Semiconductor Electrochemistry*. (Wiley VCH, 2001).
34 Gardner, R. F. G., Sweett, F. & Tanner, D. W. The electrical properties of alpha ferric oxide--II.: Ferric oxide of high purity. *J. Phys. Chem. Solids* **24**, 1183-1186 (1963).
35 Benjelloun, D. *et al.* Anisotropie des proprietes electriques de l'oxyde de fer $Fe_2O_3\alpha$. *Mater. Chem. Phys.* **10**, 503-518 (1984).
36 Read, W. T. & Shockley, W. Dislocation Models of Crystal Grain Boundaries. *Phys. Rev.* **78**, 275 (1950).
37 Blatter, G. & Greuter, F. Carrier transport through grain boundaries in semiconductors. *Phys. Rev. B* **33**, 3952 (1986).
38 Cesar, I., Sivula, K., Kay, A., Zboril, R. & Graetzel, M. Influence of feature size, film thickness, and silicon doping on the performance of nanostructured hematite photoanodes for solar water splitting. *J. Phys. Chem. C* **113**, 772-782 (2009).
39 Mohapatra, S. K., John, S. E., Banerjee, S. & Misra, M. Water Photooxidation by Smooth and Ultrathin α-Fe_2O_3 Nanotube Arrays. *Chem. Mater.* **21**, 3048-3055 (2009).
40 Rangaraju, R. R., Panday, A., Raja, K. S. & Misra, M. Nanostructured anodic iron oxide film as photoanode for water oxidation. *J. Phys. D-Appl. Phys.* **42**, 135303 (2009).
41 Sanchez, C., Sieber, K. D. & Somorjai, G. A. The photochemistry of niobium doped α-Fe_2O_3. *J. Electroanal. Chem.* **252**, 269-290 (1988).
42 Gonçalves, R. H., Lima, B. H. R. & Leite, E. R. Magnetite Colloidal Nanocrystals: A Facile Pathway To Prepare Mesoporous Hematite Thin Films for Photoelectrochemical Water Splitting. *J. Am. Chem. Soc.* **133**, 6012-6019 (2011).
43 Sivula, K. *et al. J. Am. Chem. Soc.* **132**, 7436-7444 (2010).
44 Orton, J. W. & Powell, M. J. The Hall effect in polycrystalline and powdered semiconductors. *Rep. Prog. Phys.* **43**, 1263-1307 (1980).

Acknowledgments The authors acknowledge support of this research by the European Commission (Nanostructured Photoelectrodes for Energy Conversion, NanoPEC, contract number 227179) and the Swiss Federal Office for Energy (PECHouse Competence Center, contract number 152933). We thank Elijah Thimsen, Christoph Koch, Thomas Mason, Ulrich Wiesner, Daniel Gamelin, Mark Hersam, and Roel van de Krol for helpful discussions.

Author contributions S.C.W. conceived most experiments and performed the electrochemical and electron microscopy measurements. K.V. performed the C-AFM measurements, performed statistical analyses and, with F.S., analyzed these results. A.R. and H.D. conceived and developed the photocurrent model. S.C.W. and C.H. analyzed the DF-TEM data. C.M.L. measured the macroscopic electrical properties of electrodes. M.C. prepared electrodes. S.C.W. and M.G. analyzed the electrochemical data. S.C.W. wrote most of the manuscript; K.V. wrote sections on C-AFM. All authors contributed to revisions.

Additional Information Supplementary information is available in the online version of the paper. Reprints and permissions information is available online at www.nature.com/reprints. Correspondence and requests for materials should be addressed to S.C.W.

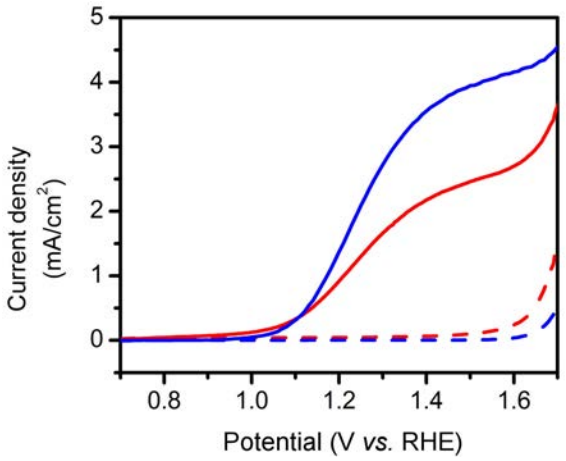

Figure 1 | Photoelectrochemical response of nanostructured hematite electrodes. The plot displays the photocurrent (solid lines) and dark current (dashed lines) for the 2L (red) and 6L (blue) electrodes.

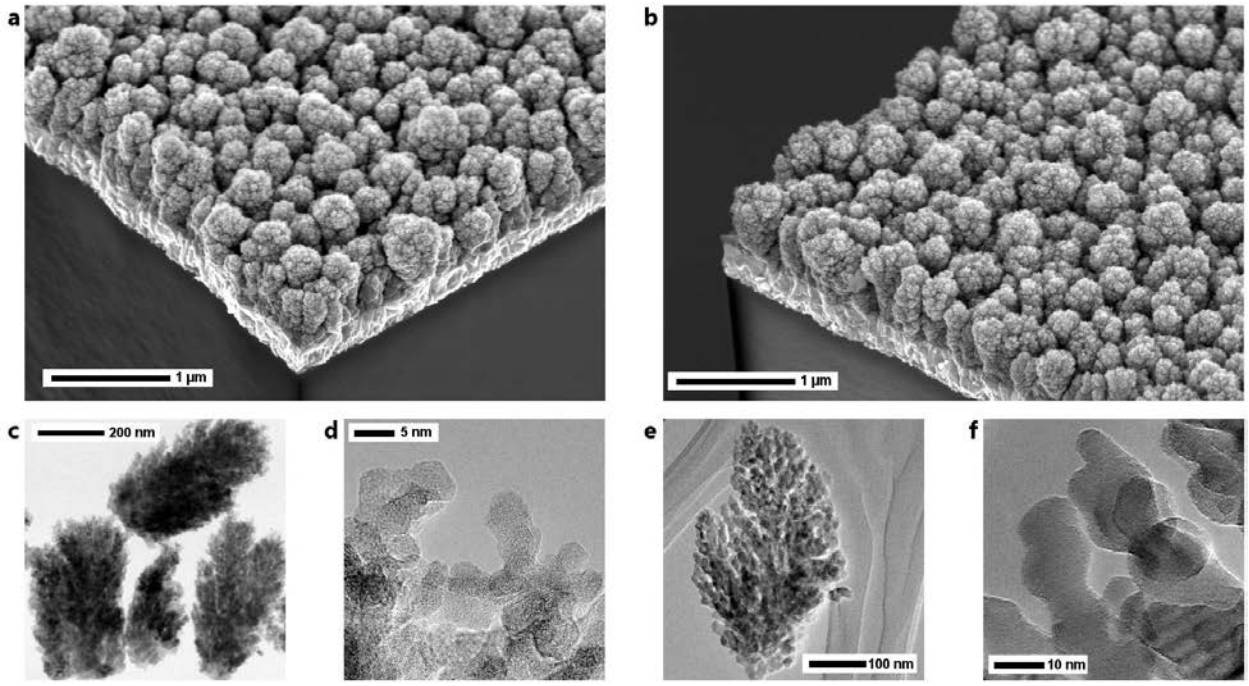

Figure 2 | Classical structure analysis by SEM and BF-TEM. Cross sectional SEM images of hematite films viewed from a 45° angle of 2L, **a,** and 6L, **b,** electrodes. The areal densities of nanoparticle aggregates (1 aggregate per 0.27 µm square for 2L and per 0.26 µm square for 6L) differed by a statistically insignificant amount (the two-tailed p-value was 0.37); the lengths (500 nm) were also similar. **c-f,** TEM images of nanoparticle aggregates that have been removed from the films and are supported on continuous carbon **c**,**d,** or lacey carbon **e,f**. Nanoparticle aggregates removed from the 2L **c**,**d** and 6L **e**,**f** electrodes.

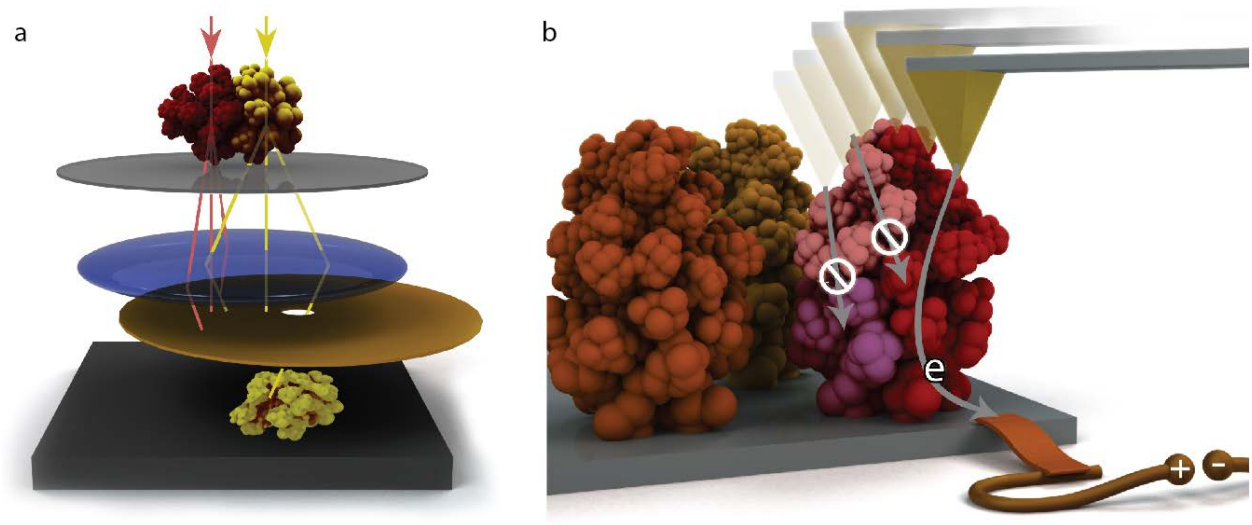

Figure 3 | Identification of champion nanostructures. a, A dark-field (DF)-TEM analysis allows each region of a nanoparticle aggregate with a unique crystallographic orientation to be imaged separately. Incident electrons (red and yellow lines) pass through two regions of a nanoparticle aggregate that have two distinct crystalline orientations (red, yellow). The incident electrons are diffracted into multiple beams, of which just three are shown for each crystalline region. The electrons pass through a transparent sample support (grey), are focused through a lens (blue) and selected using an aperture (orange). A two-dimensional projected image of the yellow region of the nanoparticle aggregate is produced on a viewing screen (black). Moving the aperture allows the selection of different diffracted beams. **b,** Analysis by conducting-atomic force microscopy (C-AFM) examines the charge transport properties of individual nanostructures. Each color represents a different crystal orientation.

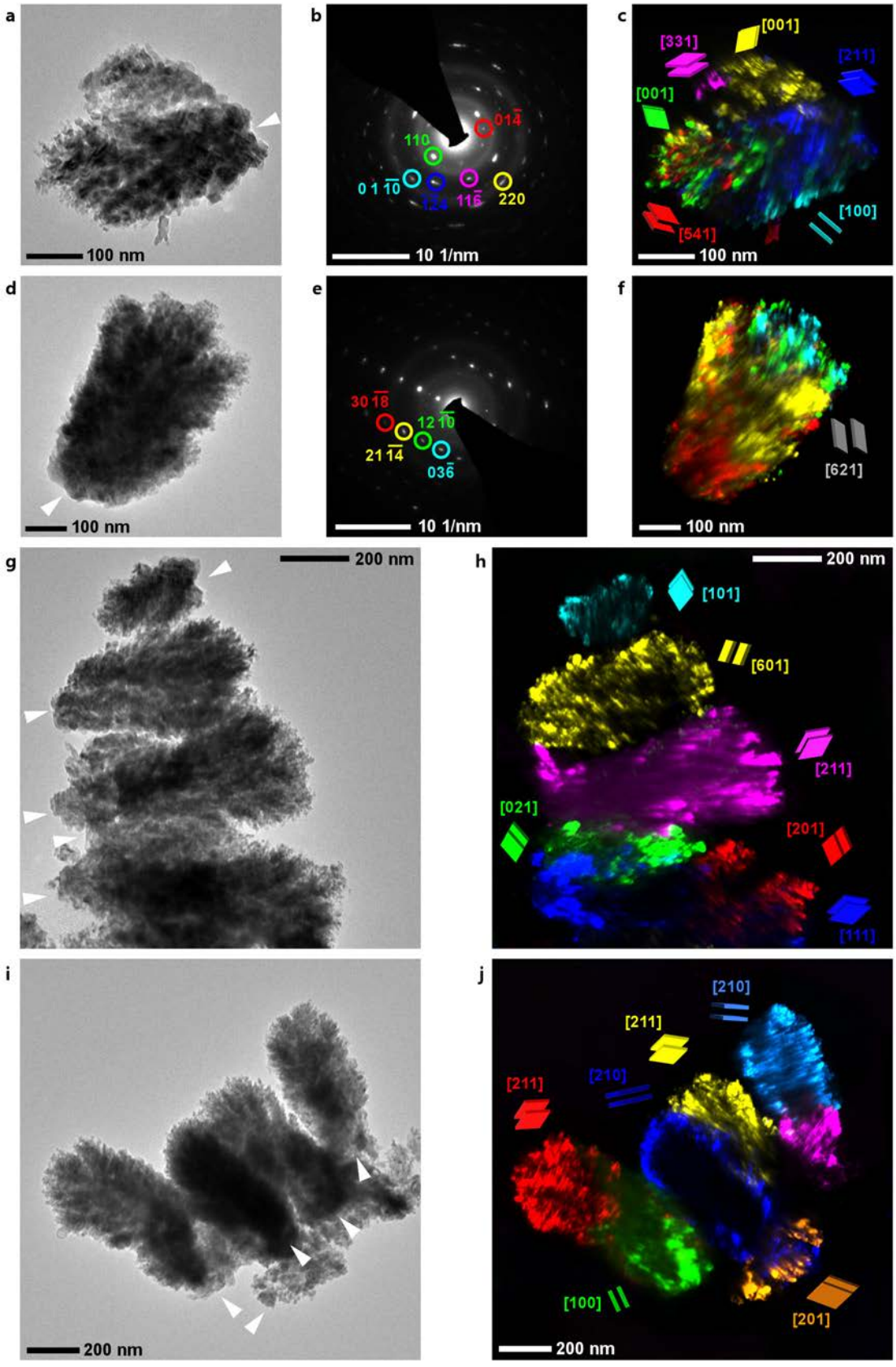
a
100 nm
b
$01\bar{4}$
110
$0\,1\,\bar{1}0$
$\bar{1}24$
$11\bar{6}$
220
10 1/nm
c
[331]
[001]
[211]
[001]
[100]
[541]
100 nm
d
100 nm
e
$30\bar{1}8$
$12\,\bar{1}0$
$21\,\bar{1}4$
$03\bar{6}$
10 1/nm
f
[621]
100 nm
g
200 nm
h
200 nm
[101]
[601]
[211]
[021]
[201]
[111]
i
200 nm
j
[210]
[211]
[211]
[210]
[100]
[201]
200 nm

Figure 4 | Imaging the crystalline structure of nanoparticle aggregates. Imaging analysis of the 2L **a**-**f** and 6L **g**-**j** samples. **a**,**d** BF-TEM, **b**,**e** diffraction patterns with indexing of diffracted beams, and **c**,**f** composite DF images for two different nanoparticle aggregates. The aggregate shown in **a**-**c** has multiple distinct orientations of crystallites. The aggregate shown in **d**-**f** has one primary orientation of the crystallites. Each set of parallelograms defines the crystallographic orientation of the corresponding region of the DF-TEM. The parallelograms are oriented to be parallel to the top and bottom surfaces (a-b plane) of the hexagonal unit cell, which are also shaped as a parallelogram (see Supplementary Fig. S2) and therefore define the directions of highest electronic mobility. **g**,**h** Bright field TEM images and **i**,**j** corresponding composite DF-TEM images of the 6L sample. The magenta mosaic in **j** is unlabeled because of the complexity of its diffraction pattern (see Supplementary Fig. S7). The region of contact that each nanoparticle aggregate made with the substrate is annotated in the BF-TEM images by a white arrowhead.

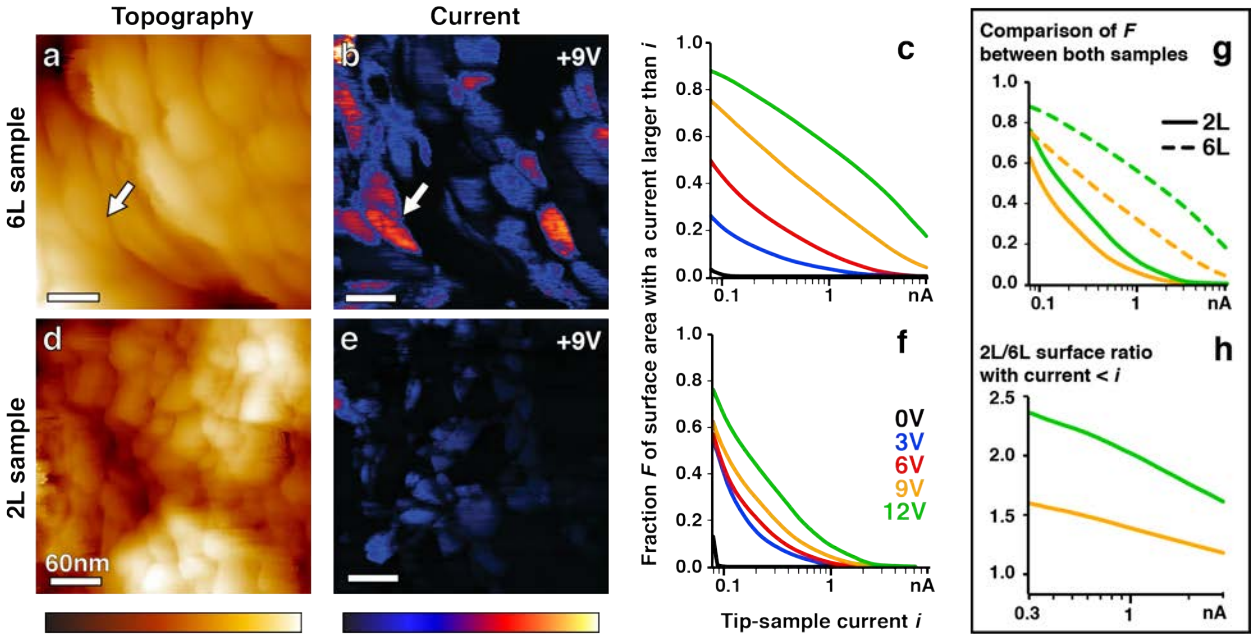

Figure 5 | Analysis of charge transport by conducting atomic force microscopy. The images show **a,d** topography and **b,e** current maps at a tip-sample voltage of 9 V. The color scales represent a total height variation of (**a)** 140 nm and (**d)** 100 nm and a current variation from 0 (black) to 5 nA (**b, e**). Regions with similar current can often be correlated with topographic features, such as the 50 × 200 nm^2 region with low current in the lower half of Fig. 5a,b, indicated by a white arrow. **c,f,** Statistical analyses of the current maps: the curves represent the fraction *F* of the surface area exhibiting a current larger than the current *i* displayed on the horizontal axis, for different applied voltages. Direct comparison of the curves obtained for both samples is provided in **g** for 9 V (orange) and 12 V (green). The 3 V and 6 V measurements are not shown because only a small proportion of the areas is above the noise level of 0.3 nA. The ratio of surface attributed to grain boundaries (with current lower than *i*, see text) is given in **h** for 0.3 nA < *i* < 3 nA. The data in **c**,**f**,**g,** and **h** represent statistics from over 10 locations for each sample. Note the log-scale for the current in these plots. Similar results could be obtained on the same samples with a Au-coated tip (Supplementary Fig. S12).

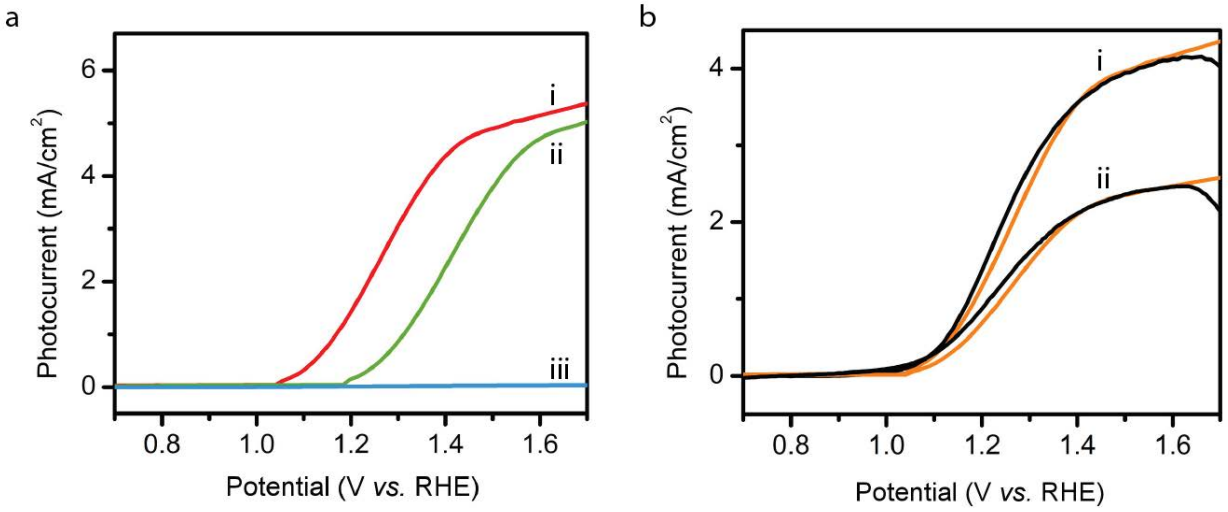

Figure 6 | Modeling the water splitting photocurrent for electrodes with grain boundaries. The photocurrent model accounts for thermionic emission over a potential barrier as well as the reduced potential drop at the electrode-electrolyte space charge layer due to the potential drop at the grain boundary. **a,** The model predicts that the photocurrent depends on the grain boundary's interface state concentration. Three scenarios are calculated: (i) no grain boundary (interfacial charge density, $Q_i = 0$), (ii) a modest interfacial state density ($Q_i = 5 \times 10^{13}$ cm^{-2}), and (iii) a high interfacial state density ($Q_i = 9 \times 10^{13}$ cm^{-2}). **b,** Comparison of 6L (i) and 2L (ii) electrodes. Experimental data (black) was obtained by subtracting the dark current from the photocurrent. The modeled data (orange) is a linear combination of the photocurrent for an electrode without grain boundaries (Fig. 6A, trace i) and an electrode in which all current must pass a grain boundary (**a**, trace iii).